


# Study and development of rear-emitter Si heterojunction solar cells and application of direct copper metallization

Lifei Yang<sup>1,2†</sup>  | Sihua Zhong<sup>2†</sup> | Wenbin Zhang<sup>1</sup> | Xingbing Li<sup>1</sup> | Zhengping Li<sup>2</sup> | Yufeng Zhuang<sup>2</sup> | Xin Wang<sup>2</sup> | Lei Zhao<sup>3,4</sup> | Xinmin Cao<sup>5</sup> | Xunming Deng<sup>5</sup> | Qi Wang<sup>1</sup> | Wenzhong Shen<sup>2,6</sup>

<sup>1</sup>GCL System Integration Technology Co., Ltd., Suzhou 215000, China

<sup>2</sup>Institute of Solar Energy, and Key Laboratory of Artificial Structures and Quantum Control (Ministry of Education), Department of Physics and Astronomy, Shanghai Jiao Tong University, Shanghai 200240, China

<sup>3</sup>Key Laboratory of Solar Thermal Energy and Photovoltaic System of Chinese Academy of Sciences, Institute of Electrical Engineering, Chinese Academy of Sciences, Beijing 100190, China

<sup>4</sup>University of Chinese Academy of Sciences, Beijing 100049, China

<sup>5</sup>Xunlight (Kunshan) Co., Ltd., Kunshan 215300, China

<sup>6</sup>Collaborative Innovation Center of Advanced Microstructures, Nanjing 210093, China

## Correspondence

Lifei Yang and Wenzhong Shen, Institute of Solar Energy, and Key Laboratory of Artificial Structures and Quantum Control (Ministry of Education), Department of Physics and Astronomy, Shanghai Jiao Tong University, Shanghai 200240, China.

Email: ylf02@126.com; wzshen@sjtu.edu.cn

## Funding information

National Natural Science Foundation of China, Grant/Award Number: 61234005, 11474201 and 11674225; Program for Innovation and Entrepreneurship of Jiangsu Province; Post-doctoral Science Foundation of Jiangsu Province; National 863 Program, Grant/Award Number: 2011AA050502

## Abstract

We have presented a comprehensive study on the development of rear emitter silicon heterojunction (SHJ) solar cells, which shows more freedom for device optimization than the standard front emitter SHJ counterparts. The optimization of the p-type hydrogenated amorphous silicon (a-Si:H(p)) layer is liberated from the parasitic absorption issue, while the n-type hydrogenated amorphous silicon (a-Si:H(n)) layer is optimized considering the tradeoff between the light absorption loss and field-effect passivation. The front transparent conductive oxide (TCO) layer can be designed stressing on its optical properties because the lateral transport of the majority carriers at the front side of the cell is supported by the Si substrate, while the rear TCO layer is free to be tuned for suppressing the TCO/a-Si:H(p) contact resistance. A rear emitter SHJ solar cell (225.47 cm<sup>2</sup>) fabricated by industry compatible process has been achieved with an efficiency of over 22%. We have further demonstrated the replacement of screen-printed silver metallization with a low cost direct copper metallization in the rear emitter SHJ solar cells. We report an exciting 22.06% cell efficiency which is comparable to that of the screen-printed counterpart.

## KEYWORDS

copper metallization, heterojunction, rear emitter, silicon, solar cell

## 1 | INTRODUCTION

Silicon heterojunction (SHJ) solar cells have gained much attention in recent years because of their high efficiency, small temperature coefficient, and simple fabrication processes.<sup>1–3</sup> For this type of cell, the

highest reported efficiency is 25.1% with a normal front emitter and bicontact structure.<sup>4</sup> Recently, the SHJ solar cells with interdigitated back contacts have been demonstrated for a photoconversion efficiency over 26% with a 180.4 cm<sup>2</sup> designated area,<sup>5</sup> confirming the strong potential of SHJ device architecture to realize high efficiency. Nevertheless, the sensitivity of cell performance to the process variations is a persistent concern for the large-scale production of the SHJ solar cells.<sup>6</sup> In this respect, the rear emitter SHJ solar cell shows

<sup>†</sup>These authors contributed equally to this work

more advantages than the front emitter counterpart because it allows an increased degree of freedom for design and optimization and therefore adapts to a wider process window. For instance, in the front emitter structure, the doping and thickness of the a-Si:H(p) layer should be determined by considering the absorption and passivation tradeoff, whereas in the rear emitter configuration, the absorption loss of the a-Si:H(p) layer is not an issue. Furthermore, it is shown by theoretical study<sup>7,8</sup> that the requirement of the conductivity of the front transparent conductive oxide layer (TCO) is lowered for the rear emitter SHJ solar cell comparing to the front emitter counterpart, because the majority carrier transport can be supported by the n-type c-Si substrate. Recently, based on the design of the rear emitter cell, Watahiki et al<sup>9</sup> have successfully realized a 23.43% efficient SHJ solar cell by utilizing an n-type microcrystalline Si layer as the window layer instead of the normally used a-Si:H(n) layer. Kobayashi et al<sup>10</sup> have reported a rear emitter SHJ solar cell with an efficiency of 23% using an epitaxial kerfless silicon wafer substrate. However, it should be noted that the research work on the rear emitter SHJ solar cell is still limited and there lacks a competitive study for deep understanding of the design principle and process optimization of the rear emitter SHJ solar cell.

Despite the technological advantages of the SHJ solar cell, its cost, on the other hand, is much higher than that of the conventional Si solar cell.<sup>11</sup> Cost reduction is highly desirable to render this technology competitive at the mass production level. A major source of cost in the SHJ solar cell is the low-temperature silver paste, which suffers from high silver consumption comparing to the conventional high-temperature silver paste. Replacing expensive silver with inexpensive copper for the metallization of SHJ solar cells can lead to substantial cost reduction. One of the promising approaches is the use of multi-wire design.<sup>12-14</sup> This technology employs many copper wires in place of silver busbars, and the copper wires are soldered to the silver fingers at low temperature. However, the copper wire normally used in this technology is coated with a low melting point alloy layer containing indium,<sup>15</sup> which reduces the cost effectiveness of the technology. Furthermore, the silver fingers are still needed to form good electric contact with the TCO layer. Thus, the production of the SHJ solar cells still relies on the low-temperature silver paste.

In this work, we present a comprehensive study on the design and development of the rear emitter SHJ solar cells by the combination of simulation and experiment. We have achieved a 22.17% efficient rear emitter SHJ solar cell with industrially compatible processes. The a-Si:H(p) layer is optimized focusing on its passivation effect. The a-Si:H(n) layer is adjusted to reduce its absorption loss while maintaining the good field-effect passivation. The front TCO layer is tuned focusing on reducing its optical absorption, while the rear TCO layer is designed to suppress the interface resistance between the a-Si:H(p) and TCO layers. We have further investigated the possibility to metallize the rear emitter SHJ solar cell by soldering the polymer coated copper wires directly on the TCO layer. As a proof of concept, we have realized a 22.06% efficient rear emitter SHJ solar cell with the front side directly copper metallized, eliminating the use of the low-temperature silver paste completely. The present study provides a more effective approach to realize high-efficiency SHJ solar cells with low cost.

## 2 | SIMULATION AND EXPERIMENTS

### 2.1 | AFORS-HET simulation

AFORS-HET simulations have been employed to study the a-Si:H(p) emitter layer in the rear emitter SHJ solar cell. In the simulation structure, the bulk lifetime of the n-type c-Si substrate was set to 10 ms. Both acceptor-like and donor-like states consisting of exponential band tail states and Gaussian distributed dangling bond states were taken into account for all hydrogenated amorphous silicon (a-Si:H) layers, and the detailed electric parameters were set as default values in AFORS-HET. The thickness of the intrinsic hydrogenated amorphous silicon (a-Si:H(i)) and a-Si:H(n) layers was set to 3 and 5 nm, respectively. The defect states at the a-Si:H(i)/c-Si interface were assumed to be continuously distributed throughout the band gap of the c-Si with a defect density of  $1 \times 10^{10} \text{ cm}^{-2} \text{ eV}^{-1}$ . Carrier transport across the a-Si:H(i)/c-Si interface was modeled by the thermionic emission process. The TCO layers on both sides of the cell were treated as optical layers with thickness of 80 nm. The TCO/a-Si:H(p) and TCO/a-Si:H(n) contacts were modelled as MS-Schottky contacts, which were set to flat band except special explanation.

### 2.2 | Rear emitter SHJ solar cell fabrication

Six-inch ( $156 \times 156 \text{ mm}^2$ ) n-type c-Si (100) wafers with resistivity of 3 to 4  $\Omega\text{-cm}$  were used as substrates. A wet chemical process with an alkaline solution was applied to remove saw damage and create a random pyramid surface texture. The final wafer thickness was approximately 155  $\mu\text{m}$ . The textured wafers were then cleaned with a standard wet-chemical cleaning sequence of RCA 1 and 2, followed by a dip in dilute HF (1%) to remove the oxide film prior to depositing a-Si:H layers. Both a-Si:H(i)/a-Si:H(n) and a-Si:H(i)/a-Si:H(p) stack layers on front and rear sides of the cell were deposited at a substrate temperature of 200°C via PECVD technology in a cluster type ULVAC CME-400E reactor. The power density and deposition pressure were in the range of 0.3 to 0.6  $\text{W}/\text{cm}^2$  and 400 to 700 Pa. The  $[\text{SiH}_4]/[\text{H}_2]$  flow ratio was in the range of 6 to 100. Hydrogen-plasma treatment was applied both before and after a-Si:H(i) deposition. Then, 80-nm TCO layers on both sides were deposited at room temperature by using a reactive plasma deposition system installed with a 1 wt%  $\text{WO}_3$ -doped  $\text{In}_2\text{O}_3$  target. The working pressure of the process chamber was kept at around 2.25 mTorr during deposition. The oxygen partial pressure was varied from 0.20 to 0.62 mTorr through adjusting the  $\text{O}_2/\text{Ar}$  flow rate ratio. For screen-printed rear emitter cells, Ag grids on both sides were formed by screen-printing low-temperature silver paste and then cured at 200°C for 30 minutes. At the front side, 74 Ag-fingers and 4 Ag-busbars were placed, while at the rear side, 200 Ag-fingers and 4 Ag-busbars were placed. For the proof of concept of direct copper metallized rear emitter cells, the front side was metallized by soldering polymer coated copper (C/Cu) wires on TCO layer directly, while the rear side was screen printed as described above.

### 2.3 | Characterization

The effective lifetime of the cell precursors was measured by Sinton lifetime tester (WCT-120) using transient photocurrent decay at an

excess carrier density of  $1 \times 10^{15} \text{ cm}^{-3}$  after the wafers are passivated by a-Si:H(i)/a-Si:H(n) and a-Si:H(i)/a-Si:H(p) stack layers on front and rear sides, respectively. The extinction coefficient of the a-Si:H layers was extracted from spectroscopic ellipsometry measurements using a Tauc-Lorentz model. For TCO layers, the sheet resistance was determined by 4-probe measurement; the carrier mobility and density were evaluated by Hall-effect measurement with the van der Pauw configuration. The extinction coefficient was obtained by fitting ellipsometry data with a Drude-Tauc-Lorentz model. The work function was measured by the Kelvin probe force microscopy technology using a Bruker Dimension Icon atomic force microscopy system. The specific contact resistances between Ag-grid, C/Cu wire, and TCO layer were measured by the transfer length measurement (TLM) method. A series of Ag-grid or C/Cu wire contacts separated by various distances ( $D$ ) were formed on TCO layer, and the resistances ( $R$ ) between them were measured. The specific contact resistance then can be extracted from the intercept of the linear plot  $R$  against  $D$ . The current-voltage ( $I$ - $V$ ) characteristics of the SHJ solar cells were measured under standard test condition with a steady-state solar cell  $I$ - $V$  tester (Industrial Vision Technology, VS-6820) equipped with a class AAA solar simulator. For the 4 busbar screen-printed solar cell, the  $I$ - $V$  tester was calibrated using a 4 busbar certified monocrystalline Si reference cell traced to Fraunhofer ISE, and the cell temperature was controlled at  $25 \pm 0.5^\circ\text{C}$ . For the direct copper metallized solar cell, the  $I$ - $V$  measurement was used to determine the  $V_{\text{OC}}$  and  $FF$ . The  $J_{\text{SC}}$  of the solar cell, however, would be overestimated if the same calibration method was used as its screen-printed counterpart. This is because that the probes pointed on the 2 solder ribbons outside the solar cell cause no light shading on the cell at all, which is unlike the case for screen-printed solar cell. To get an accurate  $J_{\text{SC}}$  value for the direct copper metallized solar cell, a full area spectral response (SR) measurement was carried out. The large-area ( $180 \times 180 \text{ mm}^2$ ) irradiance-mode SR measurement system (Industrial Vision Technology, PVE300-IVT) was calibrated by a certified monocrystalline Si reference cell as well. During the measurement, the cell was put in the middle of the  $180 \times 180 \text{ mm}^2$  light spot

with the area outside the cell covered by black paper completely to avoid unexpected light reflection and/or scattering onto the cell.

### 3 | RESULTS AND DISCUSSION

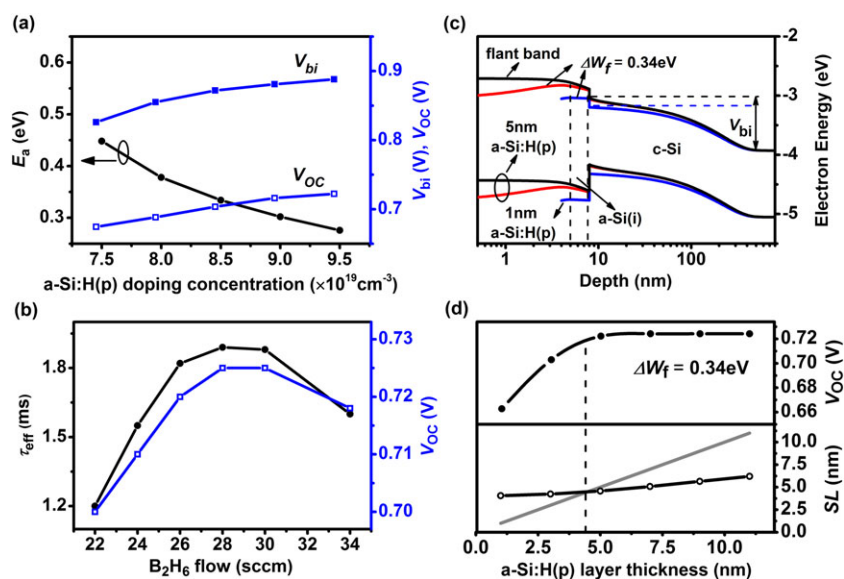
#### 3.1 | a-Si:H(p) layer optimization.

AFORS-HET simulations have been employed to reveal the design principles of the a-Si:H(p) emitter layer regarding its doping and thickness. As shown in Figure 1A, sufficient doping of the a-Si:H(p) layer should be chosen to enhance the open circuit voltage ( $V_{\text{OC}}$ ) of the rear emitter SHJ solar cell. The activation energy ( $E_a = E_F - E_V$ ) of the a-Si:H(p) layer, which is the energy gap between the Fermi level and the valence band edge, decreases with doping concentration. This leads to an increase of the built-in voltage ( $V_{\text{bi}}$ ) in c-Si near the a-Si:H/c-Si interface and a decreased saturation current of interface recombination ( $J_{0,\text{it}}$ )<sup>16</sup> according to

$$J_{0,\text{it}} = qS_{\text{it}}N_{\text{D}} \exp\left(\frac{-qV_{\text{bi}}}{kT}\right) \quad (1)$$

Here,  $q$  denotes the elementary charge,  $S_{\text{it}}$  is the recombination rate at a-Si:H/c-Si interface,  $N_{\text{D}}$  is the doping concentration of c-Si substrate, and  $kT$  is the thermal energy. Therefore, the  $V_{\text{OC}}$  of the solar cell increases with the a-Si:H(p) doping due to the suppression of emitter recombination. Experimentally, we try to control the doping of the a-Si:H(p) layer by adjusting the doping gas ( $\text{B}_2\text{H}_6$ ) flow. As shown in Figure 1B, the effective lifetime ( $\tau_{\text{eff}}$ ) and  $V_{\text{OC}}$  of the rear emitter SHJ solar cell increase with the  $\text{B}_2\text{H}_6$  flow from 22 to 26 sccm and then saturate when the  $\text{B}_2\text{H}_6$  flow reaches 28 to 30 sccm. The increase of the  $\tau_{\text{eff}}$  and  $V_{\text{OC}}$  is due to the enhanced emitter passivation, which is consistent with the simulation results. Nevertheless, when the  $\text{B}_2\text{H}_6$  flow further increases to 34 sccm, the  $\tau_{\text{eff}}$  and  $V_{\text{OC}}$  drop from their saturate value of 1.9 ms and 0.725 V to 1.6 ms and 0.718 V, respectively. This behavior is due to the fact that increasing doping creates increasing

**FIGURE 1** (A) Simulation study on the dependence of  $E_a$  of the a-Si:H(p) layer,  $V_{\text{bi}}$  in c-Si near the a-Si:H/c-Si interface, and  $V_{\text{OC}}$  of the rear emitter SHJ solar cell on the doping concentration of the a-Si:H(p) layer. Herein, the thickness of a-Si:H(p) layer is set to 5 nm. (B) Experimental results about the variation of  $\tau_{\text{eff}}$  and  $V_{\text{OC}}$  of the rear emitter SHJ solar cell with the  $\text{B}_2\text{H}_6$  flow. Simulation study of (C) the energy band diagram of the rear emitter SHJ solar cells at equilibrium with 5 or 1-nm a-Si:H(p) layers, and (D) the variation of SL of the a-Si:H(p) layer and  $V_{\text{OC}}$  of the rear emitter SHJ solar cell with the a-Si:H(p) layer thickness. The grey line is diagonal line. Herein, the a-Si:H(p) doping is set to  $9.5 \times 10^{19} \text{ cm}^{-3}$  corresponding to  $E_a$  of 0.28 eV; the  $\Delta W_{\text{f}}$  between the TCO and a-Si:H(p) layers is set to 0.34 or 0 eV (flat band), respectively [Colour figure can be viewed at [wileyonlinelibrary.com](http://wileyonlinelibrary.com)]



defects in the a-Si:H(p) layer, which may counteract the effective doping and thus reduce the field-effect passivation of the emitter. Moreover, this doping (Fermi-level) induced defect formation effect can also lead to the reduced chemical passivation of the a-Si:H(i) layer.<sup>17,18</sup>

Both effects will cause the increase of the interface recombination rate and thus the decrease of  $V_{OC}$ . The observation of  $V_{OC}$  decrease with higher a-Si:H(p) doping cannot be reflected by the simulation because there lacks such a Fermi-level dependent defect generation module for a-Si:H layers in the AFORS-HET program. In summary, there exists an optimal range for the doping of a-Si:H(p) layer, which can be controlled by the doping gas flow, to obtain a high  $V_{OC}$  for the rear emitter SHJ solar cell.

In the SHJ solar cell, the work function ( $W_f$ ) of the TCO layer is typically lower than that of the a-Si:H(p) layer. This leads to a parasitic band bending in the a-Si:H(p) layer, which is opposite to the band bending in c-Si substrate. If the whole a-Si:H(p) layer is penetrated by the parasitic band bending effect, the  $V_{bi}$  in c-Si will be counteracted, which will in turn cause  $V_{OC}$  reduction because of the similar mechanism described earlier. The screening length ( $SL$ ) of the a-Si:H(p) layer defines the characteristic length that would be required to screen the parasitic band bending.<sup>19</sup>

$$SL = 2 \cdot \sqrt{\frac{\epsilon_0 \epsilon_r kT}{2q^2 |Q_{tot,a-Si:H(p)}|}} \cdot \sqrt{\frac{q|\Delta W_f|}{kT}} \quad (2)$$

Here,  $\epsilon_0 \epsilon_r$  represents the dielectric coefficient of silicon,  $Q_{tot,a-Si:H(p)}$  is the integral average total charge density within the a-Si:H(p) layer, and  $\Delta W_f$  is the work function mismatch between the TCO and a-Si:H(p) layers. Figure 1C shows the simulated energy band diagrams of rear emitter SHJ solar cells with the a-Si:H(p) layers under variable  $\Delta W_f$ . It is found that the solar cell with a 5-nm a-Si:H(p) layer can screen the parasitic band bending effectively, while the solar cell with a 1-nm a-Si:H(p)

suffers from a reduction of  $V_{bi}$ . Figure 1D investigates the variation of  $SL$  of the a-Si:H(p) layer and  $V_{OC}$  of the rear emitter cell with the a-Si:H(p) layer thickness. Here, the a-Si:H(p) doping is set to  $9.5 \times 10^{19} \text{ cm}^{-3}$  corresponding to  $E_a$  of 0.28 eV, and the  $\Delta W_f$  is set to 0.34 eV. It can be seen that the  $V_{OC}$  becomes saturated only when the thickness of the Si(p) layer exceeds its  $SL$ , which is consistent with the results shown in Figure 1C. Based on earlier results, it is clear that there is a minimum thickness of a-Si:H(p) layer required to screen the parasitic band bending effect and thereby maintain the  $V_{OC}$  of the solar cell.

Figure 2 shows the variation of photovoltaic parameters of the rear emitter SHJ solar cells with the deposition time of the a-Si:H(p) layer, which is proportional to the layer thickness. It can be observed that the  $V_{OC}$  of the solar cells increases with the deposition time and nearly saturates at 25 seconds. We attribute this observation to a better passivation of the a-Si:H(p) emitter because of the improved shielding of the parasitic band bending and may be the enhanced effective doping of the a-Si:H(p) layer as its thickness increasing.<sup>20</sup> The fill factor ( $FF$ ) of the solar cells shows a trend of first increase and then decrease. Note that both the recombination and series resistance ( $R_s$ ) can impact  $FF$ . Pseudo  $FF$  ( $pFF$ ) of the solar cells is collected by Suns- $V_{OC}$  measurement to see the recombination related  $FF$  variation. It is clear that the  $pFF$  shows a similar trend to the  $V_{OC}$ , which can be attributed to a better passivation quality for thicker a-Si:H(p) emitter. The  $R_s$  of the solar cells can then be extracted using the following relationship,<sup>21</sup> where  $J_{mpp}$  is the current density of the solar cell at the maximum power point.

$$R_s = (pFF - FF) \frac{V_{OC} J_{SC}}{J_{mpp}^2} \quad (3)$$

It is found that the  $R_s$  increases with the deposition time of the a-Si:H(p) layer. Therefore, the  $FF$  trend is caused by the competition between the improved passivation and the increased parasitic series

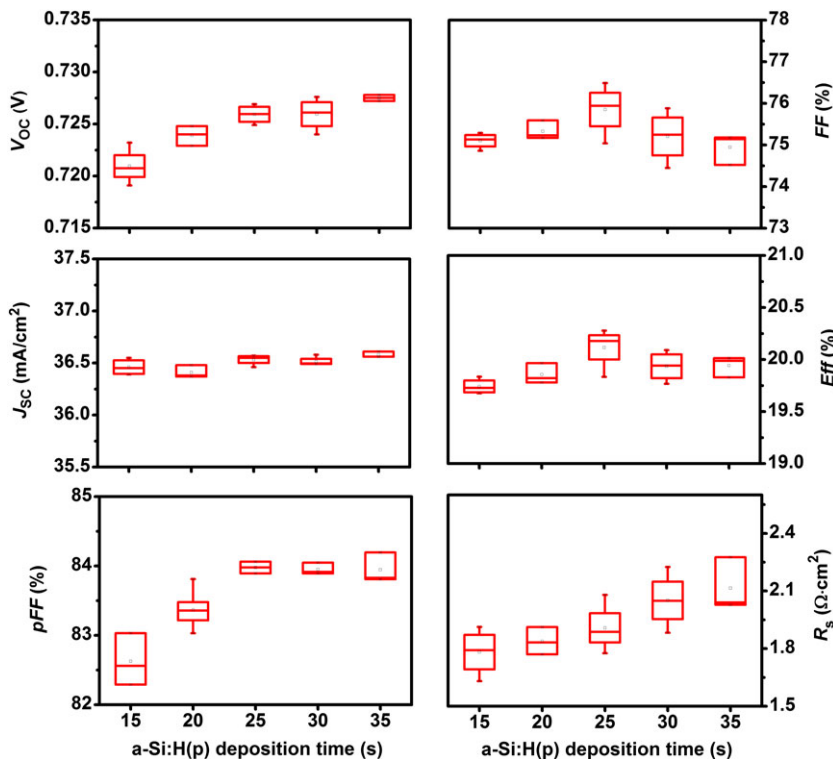


**FIGURE 2** Variation of the photovoltaic parameters ( $V_{OC}$ ,  $J_{SC}$ ,  $FF$ ,  $Eff$ ,  $pFF$ , and  $R_s$ ) of the rear emitter SHJ solar cells with the deposition time of the a-Si:H(p) layer [Colour figure can be viewed at wileyonlinelibrary.com]

resistance as the a-Si:H(p) thickness increasing. The  $J_{SC}$  of the solar cell is independent of the a-Si:H(p) thickness, which is expected for the rear emitter configuration. Consequently, there is an optimal a-Si:H(p) thickness, corresponding to deposition time of 25 seconds here, for the rear emitter SHJ solar cell to achieve the highest efficiency ( $Eff$ ).

To evaluate the thickness of the a-Si:H(p) layer, we grow a thick a-Si:H(p) layer on glass substrate and measure its thickness with the spectroscopic ellipsometry using a Tauc-Lorentz model, from which the average deposition rate of the a-Si:H(p) layer on glass is extracted. The average deposition rate of a-Si:H(p) layer on the pyramidally textured Si surface is obtained by dividing the deposition rate on glass by a geometrical factor of 1.33, which will be determined in Section 3.3. Through the measurements and calculations, the depositing rate of the a-Si:H(p) is estimated to be 0.44 nm/s, and the optimized thickness of the a-Si:H(p) layer is 11 nm for our state-of-the-art process.

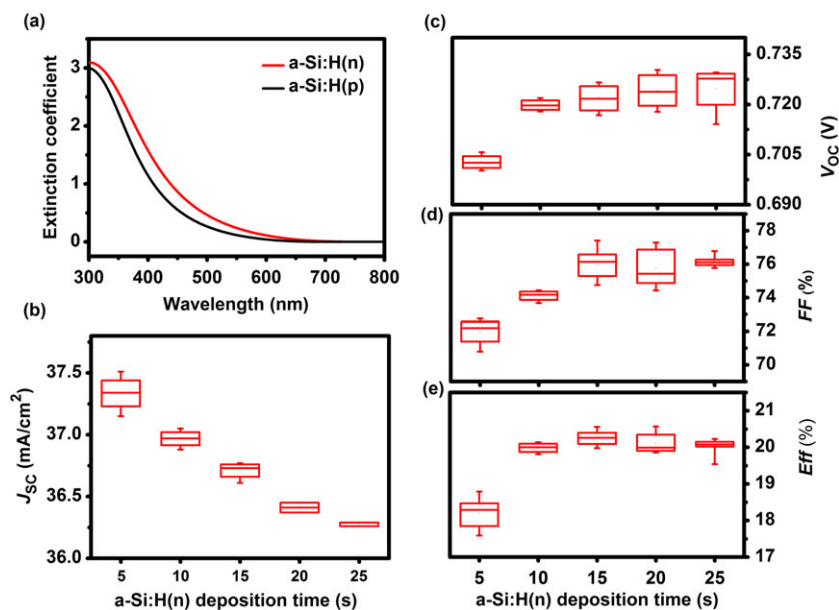
### 3.2 | A-Si:H(N) LAYER OPTIMIZATION

Figure 3A shows the extinction coefficients of the a-Si:H(n) and a-Si:H(p) layers deposited by our state-of-the-art process for SHJ solar cells. It is found that the a-Si:H(n) layer has a larger extinction coefficient than the a-Si:H(p) layer, indicating its stronger optical absorption. This result is consistent with the study of Holman et al.<sup>22</sup> Therefore, the parasitic light absorption of the a-Si:H(n) layer must be well controlled to enhance the  $J_{SC}$  of the rear emitter SHJ solar cell. As shown in Figure 3B, the  $J_{SC}$  can be effectively improved by reducing the thickness of the a-Si:H(n) layer through cutting its deposition time. In Figure 3C-E, the dependence of other photovoltaic parameters ( $V_{OC}$ ,  $FF$ ,  $Eff$ ) of the rear emitter SHJ cell on a-Si:H(n) deposition times is investigated. It is noticed that the  $V_{OC}$  and  $FF$  increase with the a-Si:H(n) deposition time and saturate at 15 seconds, which can be attributed to a better field-effect passivation for a thicker a-Si:H(n) layer. Nevertheless, there is no obvious  $FF$  reduction when the deposition time of a-Si:H(n) layer increases from 15 to 25 seconds, demonstrating that the increase of series resistance caused by thicker a-Si:H(n) layer is insignificant here because of the relatively low resistivity of a-Si:

H(n). The tradeoff among the  $V_{OC}$ ,  $FF$ , and  $J_{SC}$  determines an optimized a-Si:H(n) layer thickness for the rear emitter SHJ solar cell to achieve the highest efficiency (see Figure 3E), which is estimated to be approximately 7 nm (corresponding to deposition time of 15 seconds) by using the same method described in Section 3.1.

### 3.3 | Front TCO layer optimization

The front TCO layer is the window layer for the rear emitter SHJ solar cell, and its optical and electrical properties should be well tuned to improve the efficiency of the cell. Here, we try to optimize the front TCO layer property by adjusting the oxygen partial pressure, which is the most important parameter for TCO deposition. Figure 4A shows the variation of the TCO sheet resistance ( $R_{sheet,TCO}$ ) with the oxygen partial pressure, measured both on glass and at the rear side of the cell after a 200°C/30 minute annealing treatment. It can be found that the  $R_{sheet,TCO}$  increases with the oxygen partial pressure, which is due to the decrease of the carrier density in the TCO layer with its mobility stabilizing at approximately 55 cm<sup>2</sup>/Vs (see Figure 4B). It is also noticed that the  $R_{sheet,TCO}$  on glass is lower than that on the cell, which should be mainly due to the different TCO thickness on flat glass and on a textured wafer determined by the geometrical factor of the texture structure. Besides, it is also reported that the hydrogen effusing from a-Si:H layers due to thermal treatment can dope the TCO in SHJ solar cells.<sup>23</sup> To identify if this effect exists in our rear emitter SHJ solar cells, TCO samples deposited on a-Si:H(p)/a-Si:H(i)/glass substrates are fabricated. Note that the a-Si:H(p)/a-Si:H(i) stack layers are deposited using the same process as fabricating SHJ solar cells and the TCO is deposited at the oxygen partial pressure of 0.42 mTorr. Figure 4C shows the sheet resistance and carrier density of the TCO samples after an annealing treatment at 200°C for 30 minutes. It is indeed found that the TCO sheet resistance is decreased by approximately 15% (from 60 to 51 Ω/sq) when the substrate is switched from glass to a-Si:H(p)/a-Si:H(i)/glass, due to the increased carrier density. Through considering this hydrogen doping effect, the geometrical factor of the textured wafer is calculated to be 1.44. In the meantime,



**FIGURE 3** (A) Extinction coefficients of the a-Si:H(n) and a-Si:H(p) layers extracted from the ellipsometry measurements. (B-E) Variation of photovoltaic parameters ( $J_{SC}$ ,  $V_{OC}$ ,  $FF$ ,  $Eff$ ) of the rear emitter SHJ cells with the deposition time of the a-Si:H(n) layer [Colour figure can be viewed at [wileyonlinelibrary.com](http://wileyonlinelibrary.com)]

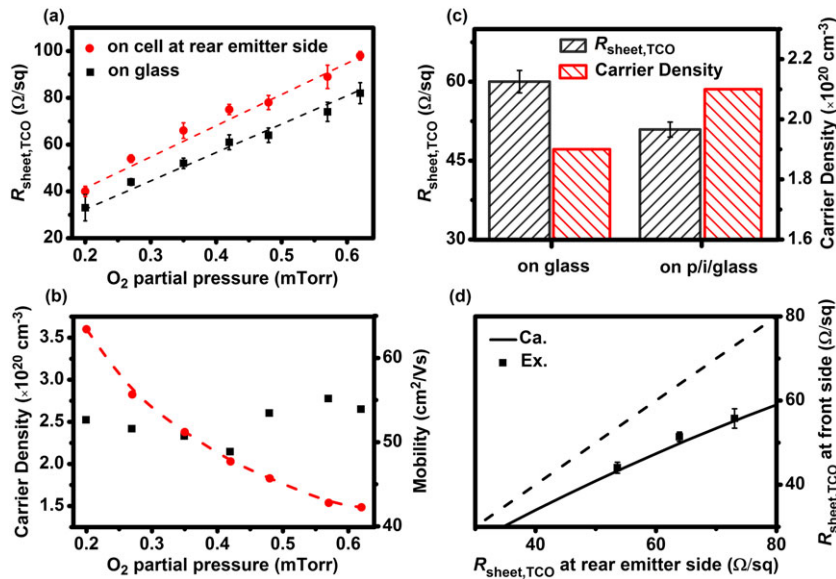


**FIGURE 4** Variation of (A) TCO sheet resistance measured on glass and at rear side of the cell, (B) carrier density and mobility of the TCO layer with oxygen partial pressure. The samples are measured after an annealing treatment at 200°C for 30 min. The dash lines are guides for the eyes. (C) Comparison of TCO sheet resistance and carrier density measured on glass and p/i/glass substrates after an annealing treatment at 200°C for 30 minutes, where i/p represents the a-Si:H(i)/a-Si:H(p) stack layers deposited using the same process as fabricating the SHJ solar cells. (D) Relationship between the  $R_{\text{sheet,TCO}}$  measured at the rear side and the front side of the cell. The solid line describes the  $R_{\text{sheet,TCO}}$  at the front side of the cell calculated by a parallel connection model of the TCO layer and the Si substrate. The dash line is diagonal line [Colour figure can be viewed at [wileyonlinelibrary.com](http://wileyonlinelibrary.com)]

the geometrical factor determined by the 3D optical microscope measurement is approximately 1.22 through comparing the textured Si surface area to the flat Si surface area. Because both of these methods are indirect and have errors, here we use the average value of 1.33 for the geometrical factor. Figure 4D further demonstrates that the  $R_{\text{sheet,TCO}}$  measured at the rear side of the cell is higher than that measured at the front side of the cell. This is because the lateral transport of the majority carriers at the front side of the cell can be shifted from the TCO layer into the n-type Si substrate thanks to the n-type conductive nature of the TCO material, which allows the electrically parallel connection of the TCO layer with the Si substrate. On the contrary, the a-Si:H(p)/c-Si(n) junction at the rear side of the cell insulates the TCO layer from the Si substrate, which means the measured  $R_{\text{sheet,TCO}}$  corresponds to that of the TCO layer itself. The solid line in Figure 4D describes the calculated  $R_{\text{sheet,TCO}}$  at the front side of the cell by a parallel model (Equation 4), which fits well to the experiment data. Here,  $R_{\text{sheet,c-Si}}$  represents the sheet resistance of the Si substrate.

$$\frac{1}{R_{\text{sheet,TCO}}(\text{front side})} = \frac{1}{R_{\text{sheet,TCO}}(\text{rear side})} + \frac{1}{R_{\text{sheet,c-Si}}} \quad (4)$$

This 2D majority carrier transport effect leads to less restriction on the conductivity of front TCO layer for the rear emitter SHJ solar cell compared with its front emitter counterpart.<sup>10</sup> Therefore, suppressing the light absorption in the front TCO layer should be more important in improving the efficiency of the rear emitter cell.

Figure 5A shows the extinction coefficients of the TCO layers deposited at various oxygen partial pressures. It can be seen that the extinction coefficient at the long wavelength range (500 to 900 nm) decreases effectively with the oxygen partial pressure from 0.20 to 0.42 mTorr and then becomes nearly stable. This is linked to the decrease of the carrier density with the oxygen partial pressure (see Figure 4B), which can reduce the free carrier absorption in the TCO layers. Consistent with the results in Figure 5A, the  $J_{\text{SC}}$  of the rear emitter cell is found to increase with the oxygen partial pressure and

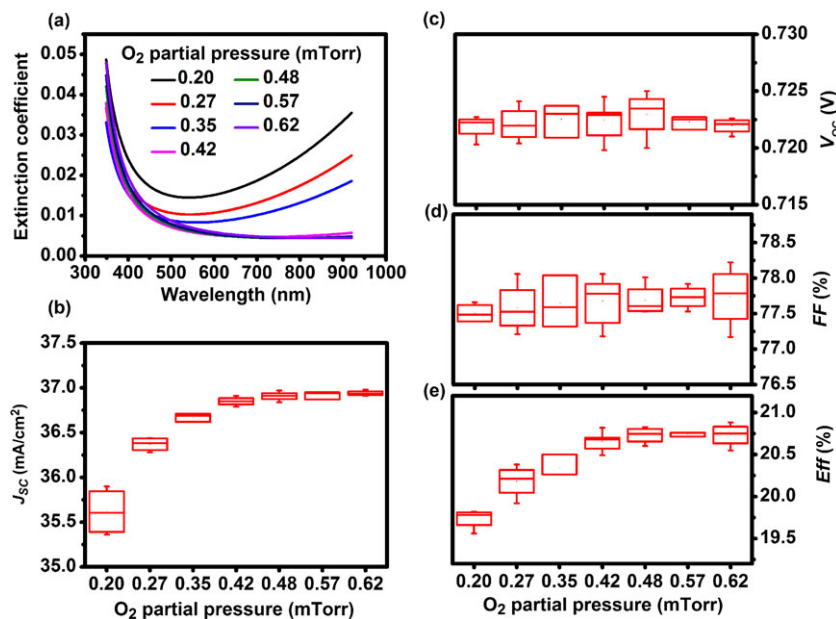


**FIGURE 5** (A) Variation of the extinction coefficients of the TCO layers deposited at various oxygen partial pressures. (B-E) Variation of photovoltaic parameters ( $J_{\text{SC}}$ ,  $V_{\text{OC}}$ ,  $FF$ ,  $Eff$ ) of the rear emitter SHJ cells with the oxygen partial pressure [Colour figure can be viewed at [wileyonlinelibrary.com](http://wileyonlinelibrary.com)]

nearly saturates at 0.42 mTorr as demonstrated in Figure 5B. Figure 5 C-E exhibits the dependence of other photovoltaic parameters ( $V_{OC}$ ,  $FF$ ,  $E_{ff}$ ) of the rear emitter cell on the oxygen partial pressure. It is noticed that the  $V_{OC}$  is independent of the oxygen partial pressure, indicating that the parasitic band bending effect described in Section 3.1 is fully screened by the a-Si:H(p) layer. Interestingly, the  $FF$  is also found to be insensitive to the oxygen partial pressure at the range from 0.20 to 0.62 mTorr although the increase of  $R_{sheet,TCO}$  with the oxygen partial pressure is expected to cause increasing resistance loss and thus decreasing  $FF$ . This apparent contradiction will be studied and explained in the next section. Consequently, the front TCO layer should be deposited at a relatively high oxygen partial pressure, no less than 0.42 mTorr in our state-of-the-art process, for the rear emitter SHJ solar cell to achieve the highest efficiency (see Figure 5E).

### 3.4 | Rear TCO layer optimization

As shown in Figure 6A, a fundamental problem when contacting a-Si:H(p) with TCO (normally n type) is the formation of an interface barrier, which precludes the hole transport from the a-Si:H(p) layer to TCO layer, and thereby gives rise to a large contact resistance between the a-Si:H(p) and TCO layers in the SHJ solar cell. Here, we apply a similar method described by Gogolin et al<sup>24</sup> to quantitatively investigate the TCO/a-Si:H(p) contact resistance ( $R_{TCO/a-Si:H(p)}$ ) and its variation with the oxygen partial pressure. To this end, symmetry structure devices (see Figure 6B) have been fabricated by depositing a-Si:H(i), a-Si:H(p) and TCO layers on both sides of the p-type c-Si substrate and metallized by screen-printing technique. Note that the deposition processes for a-Si:H(i), a-Si:H(p), and TCO layers, together with the screen-printing metallization process used for the test devices, are exactly the same as those of their rear emitter cell counterparts. Figure 6C demonstrates the linear  $J$ - $V$  characteristic of the test devices with TCO layer deposited at various oxygen partial pressures measured under 1-sun illumination, from which the total resistance ( $R_T$ ) of the test devices can be extracted. As described by Equation 5,  $R_T$  includes the  $R_{TCO/a-Si:H(p)}$ , the bulk resistance of the crystalline Si substrate ( $R_c$ -

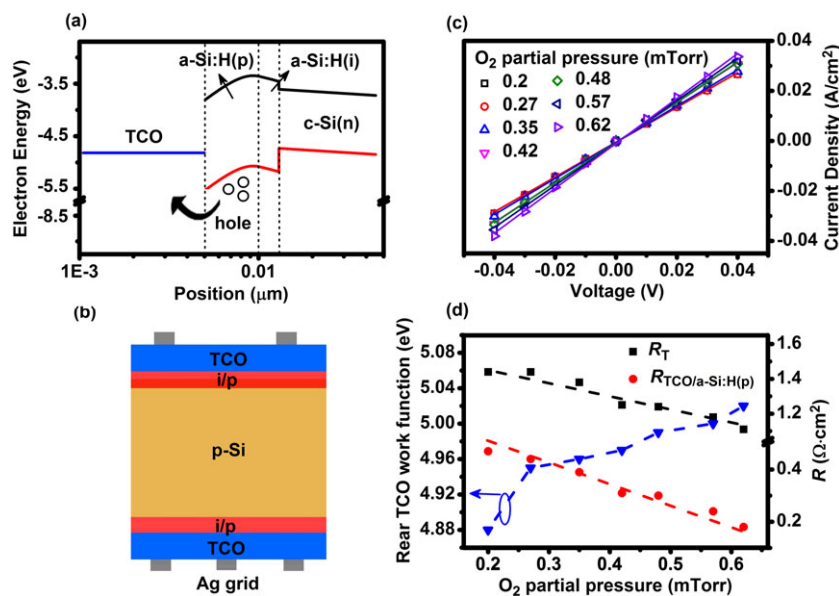
$s_i$ ), the lateral transport resistance through the front and rear TCO layers ( $R_{TCO}$ ), the lateral transport resistance through the front and rear metallization Ag-grid ( $R_{metallization}$ ), and the TCO/Ag contact resistance at the front and rear side ( $R_{TCO/Ag}$ ).

$$R_T = R_{c-Si} + R_{TCO} + R_{metallization} + R_{TCO/Ag} + 2R_{TCO/a-Si(p)} \quad (5)$$

These series resistance components can be determined by well-established methods. The  $R_{c-Si}$  is calculated by multiplying the resistivity with its thicknesses. The line resistances of the Ag-finger and Ag-busbar are measured by a resistance meter. The sheet resistance of TCO layers is determined by 4-probe measurement. The TCO/Ag specific contact resistance ( $\rho_{TCO/Ag}$ ) is measured on a TLM structure.<sup>25</sup>  $R_{TCO}$ ,  $R_{metallization}$ , and  $R_{TCO/Ag}$  are then calculated based on the unit cell approach.<sup>26</sup> With these data in hand,  $R_{TCO/a-Si:H(p)}$  is then extracted using Equation 5. Note that here the  $R_{TCO/a-Si:H(p)}$  actually includes also the bulk resistances of the a-Si:H(i) and a-Si:H(p) stack layers, which are difficult to measure due to their extremely low thickness. As shown in Figure 6D, the work function of the TCO layer increases with the oxygen partial pressure, which is consistent with the result reported by Haug et al,<sup>27</sup> while both the  $R_T$  and  $R_{TCO/a-Si:H(p)}$  decrease with the oxygen partial pressure. The  $R_{TCO/a-Si:H(p)}$  decreases from 0.47 to 0.18  $\Omega\text{-cm}^2$  as the oxygen partial pressure varies from 0.20 to 0.62 mTorr. These values of  $R_{TCO/a-Si:H(p)}$  are comparable with those previously reported values.<sup>24,28,29</sup> This result means that the  $R_{TCO/a-Si:H(p)}$  can be effectively suppressed through enhancing the work function of rear TCO layer, which reduces the interface barrier and hence facilitates the carrier tunneling and/or thermionic emission process. The opposite trend of  $R_{TCO/a-Si:H(p)}$  and  $R_{TCO,sheet}$  (see Figure 4A) with the oxygen partial pressure makes the series resistance of the solar cell insensitive to the oxygen partial pressure, which explains the behavior of the  $FF$  observed in Section 3.3.

Based on previous observation, we find a new structure design to enhance the  $FF$  of the rear emitter SHJ cell. Comparing with the reference cell with front and rear TCO layers all deposited at oxygen partial pressure of 0.42 mTorr (see Figure 7A), the TCO layer at the rear side

**FIGURE 6** (A) Energy band diagram of the SHJ solar cell highlights the hole transport through the TCO/a-Si:H(p) contact. (B) Cross-sectional schematic of the test device structure for determining the  $R_{TCO/a-Si:H(p)}$ , where p-Si, i/p represent the p-type c-Si substrate and a-Si:H(i)/a-Si:H(p) stack layers respectively. (C) Light  $J$ - $V$  measurement results of the test devices with TCO layer deposited at various oxygen partial pressures under 1-sun illumination. (D) Variation of the work function of rear TCO layer,  $R_T$  of the test devices, and the  $R_{TCO/a-Si:H(p)}$  with the oxygen partial pressure. The  $R_{TCO/a-Si:H(p)}$  here actually includes also the bulk resistances of the a-Si:H(i) and a-Si:H(p) stack layers. Symbols represent experimental data. Lines are guides for the eye [Colour figure can be viewed at [wileyonlinelibrary.com](http://wileyonlinelibrary.com)]



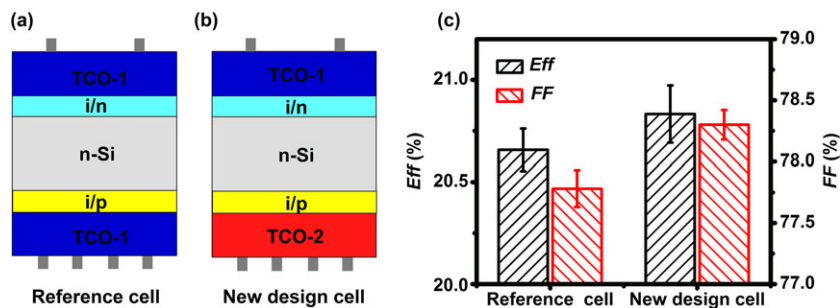


**FIGURE 7** Schematic cross section of the (A) reference and (B) new design rear emitter SHJ solar cell. TCO-1 and TCO-2 layers are deposited at the oxygen partial pressure of 0.42 and 0.62 mTorr, respectively. i/n and i/p represent the a-Si:H(i)/a-Si:H(n) and a-Si:H(i)/a-Si:H(p) stack layers, respectively. (C) Comparison of FF and Eff of the new design cell with those of the reference cell [Colour figure can be viewed at [wileyonlinelibrary.com](http://wileyonlinelibrary.com)]

of the new design cell (see Figure 7B) is deposited at high oxygen partial pressure (0.62 mTorr) to suppress the  $R_{\text{TCO/a-Si:H(p)}}$ . Note that the number of Ag-finger at the rear side is nearly 3 times of that at the front side, leading to insignificant series resistance contributing from the rear TCO layer. The TCO layer at the front side of the new design cell is deposited at a moderate oxygen partial pressure (0.42 mTorr) to control its sheet resistance and maintain the  $J_{\text{SC}}$  of the cell at a high level. Figure 7C shows the comparison of FF and Eff of the new design cell with those of the reference cell. It can be seen that the FF of the new design cell is approximately 0.5%<sub>abs</sub> higher than that of the reference cell due to the suppressed  $R_{\text{TCO/a-Si:H(p)}}$ , bringing an Eff gain of approximately 0.2%<sub>abs</sub>.

Finally, through combining all our state-of-the-art processes, namely the a-Si:H(p) layer grown under 30 sccm  $\text{B}_2\text{H}_6$  flow and 25 seconds (corresponding to  $\sim 11$  nm), the a-Si:H(n) layer grown under 15 seconds (corresponding to  $\sim 7$  nm), the front TCO layer deposited at the oxygen partial pressure of 0.42 mTorr and the rear TCO layer deposited at the oxygen partial pressure of 0.62 mTorr, we have successfully achieved 22.17% efficient rear emitter SHJ solar cell, whose light J-V curve is shown in Figure 8. Note that the area of the cell is 225.47  $\text{cm}^2$ , which is obtained by cutting the poor passivation edge area of a 6-inch cell by laser. The wavelength of the laser is 355 nm, and the power of the laser generator is less than 5 W.

### 3.5 | Application of direct copper metallization

Besides pursuing high conversion efficiency, improving economic performance is also important for the SHJ technology to gain competitive

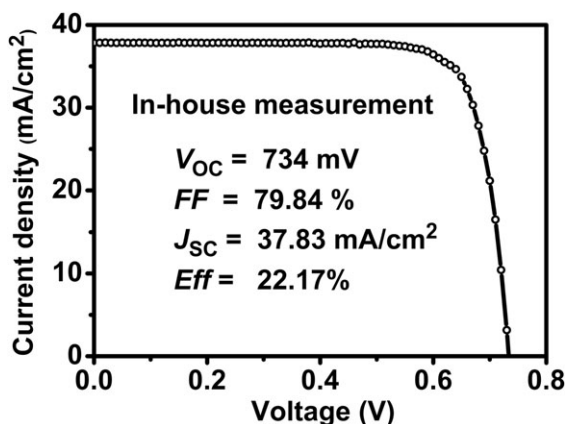


**FIGURE 8** Light J-V curve of the champion rear emitter SHJ solar cell measured in house under the standard condition (25°C, AM1.5 spectrum, 100  $\text{mW}/\text{cm}^2$ )

advantage in mass production. Replacing silver with copper for SHJ solar cell metallization can lead to effective cost reduction. Here, we try to realize direct copper metallization through multi-wire technology using polymer coated copper (C/Cu) wires soldered directly on the TCO layer of the rear emitter SHJ solar cell. The C/Cu wire (from FURUKAWA Co., Ltd.) has been successfully used for the direct metallization of amorphous silicon solar cells in Xunlight (Kunshan) Co., Ltd. However, SHJ solar cells have much larger  $J_{\text{SC}}$  than that of the amorphous silicon solar cells, meaning that their series resistance ( $R_s$ ) must be better controlled to maintain the FF at a high level. In this respect, the rear emitter solar cell has advantage because the absorber can provide an additional lateral transport path for the majority carriers, which is equivalent to reducing the sheet resistance of the front TCO layer (see Section 3.3) and thus benefits  $R_s$  suppression. The C/Cu wires are soldered on TCO by heat pressing the C/Cu wires onto the TCO layer directly at 220°C. The electric contact between the C/Cu wire and TCO is realized through the polymer coating layer of the C/Cu wire, which is conductive and containing adhesive agent that can bond with TCO under heat and pressure. Figure 9A,B shows top SEM views showing C/Cu wires soldered on the front TCO layer of the rear emitter cell. The diameter of the C/Cu wire is 150  $\mu\text{m}$ , with a copper core of 100  $\mu\text{m}$  and a polymer coating layer of 25  $\mu\text{m}$ . Figure 9C,D shows the cross-sectional SEM views of a C/Cu wire soldered on the TCO layer. It can be seen that the polymer coating layer contacts directly to the TCO and the Si pyramids penetrate into the polymer layer, facilitating the electrical contact between the C/Cu wire and the TCO. As shown in Figure 9E, the specific contact resistance between the C/Cu wire and the TCO layer is determined to be 18.6  $\text{m}\Omega\cdot\text{cm}^2$  by the TLM measurement. Meanwhile, the extracted  $R_{\text{sheet,TCO}}$  is 59  $\Omega/\text{sq}$ , consistent with the value of 56  $\Omega/\text{sq}$  determined by 4-probe measurement at the front side of the cell (see Section 3.3). Based on these measured data and the unit cell method,<sup>26</sup> we calculate that the  $R_s$  of the direct copper metallized rear emitter cell can be close to its screen-printed counterpart for our state-of-the-art process (see dash line in Figure 9F) if the number of C/Cu wires is set to ensure nearly equal shading fraction of C/Cu wires and printed Ag-fingers. Note that the  $R_s$  difference between these 2 type of cells can be further reduced if  $R_{\text{sheet,TCO}}$  at the front side of the cell can be decreased even more. To further decrease the contact resistance between the C/Cu wire and TCO, the polymer coating layer may need to be modified.

As a proof of concept, we fabricate a rear emitter SHJ cell whose front side is directly copper metallized (see Figure 10A). Figure 10B shows the photo of the cell with an area of 156.25  $\text{cm}^2$ , in which 50 C/Cu wires are soldered on the TCO layer. The average distance



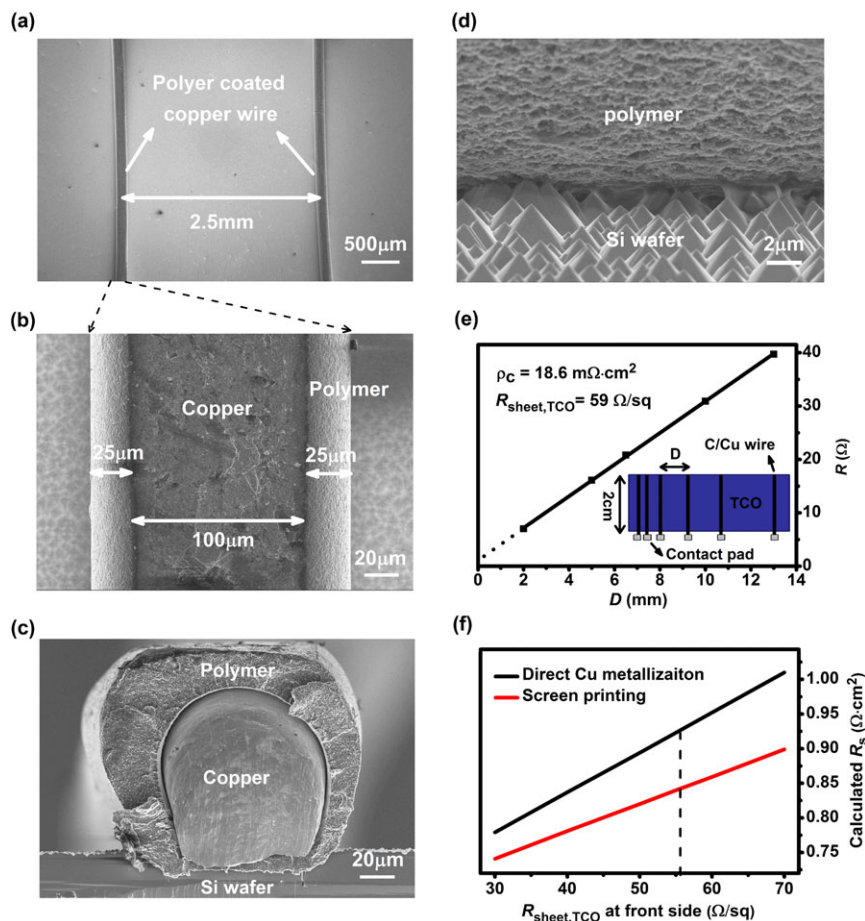


**FIGURE 9** Top SEM views (A-B) and cross-sectional SEM views (C-D) of C/Cu wire soldered on front TCO layer of the rear emitter cell. (E) Specific contact resistance between C/Cu wire and TCO layer measured by the TLM method. The inset picture shows the TLM structure. (F) Variation of calculated  $R_s$  of the direct copper metallized rear emitter cell and its screen-printed counterpart with  $R_{\text{sheet,TCO}}$  at the front side of the cell. The dash line indicates  $R_{\text{sheet,TCO}}$  for our state-of-the-art process. Herein, the number of C/Cu wire is set to ensure nearly equal shading fraction of C/Cu wires and printed Ag-fingers for direct copper metallized cell and its screen-printed counterpart [Colour figure can be viewed at [wileyonlinelibrary.com](http://wileyonlinelibrary.com)]

between the C/Cu wires is approximately 2.5 mm (see Figure 9A). The shading fraction of 50 C/Cu wires for the copper metallized solar cell is 6.0%. Note that the shading fraction of 74 Ag fingers (70  $\mu\text{m}$ ) and 4 Ag busbars (1.1 mm) for the 6-inch screen-printed solar cell is 6.1% and the laser cut is performed symmetrically in the middle of the cell, which will not change the shading fraction. Therefore, the direct copper metallized solar cell and the screen-printed solar cell nearly have equal optical shading loss. Two solder ribbons with width of 8.0 mm and thickness of 0.2 mm are placed at the side of cell for  $I$ - $V$  measurement. Figure 10C shows the EL image of the cell, from which the C/Cu wires can be clearly identified, indicating good electric contact between the C/Cu wire and TCO and that the current extraction is homogeneous over the whole cell. Figure 10D shows the full area SR of the cell and the integrated  $J_{\text{SC}}$  calculated by integrating the SR with AM 1.5G spectrum. The  $J_{\text{SC}}$  of the cell is thus determined to be 37.84  $\text{mA}/\text{cm}^2$ . As shown in Figure 10E, this cell achieves an  $\text{Eff}$  of 22.06% ( $V_{\text{OC}} = 737$  mV,  $J_{\text{SC}} = 37.84$   $\text{mA}/\text{cm}^2$ ,  $\text{FF} = 79.10\%$ ). The  $V_{\text{OC}}$  and  $J_{\text{SC}}$  of this cell are comparable to those of its screen-printed counterpart (see Figure 8), while  $\text{FF}$  is a little bit lower, which is consistent with the  $R_s$  calculation result (see Figure 9F). Note that the approach of direct metallization of SHJ solar cells has been reported in the work of Faes et al,<sup>12</sup> in which they use InSn-coated copper (InSn/Cu) wire to contact TCO directly and get a 19.9% efficient single cell mini-module ( $V_{\text{OC}} 0.734$  V,  $J_{\text{SC}} 37.3$   $\text{mA}/\text{cm}^2$ ,  $\text{FF} 74.0\%$ ). In our case, C/Cu wires are used for the direct metallization of SHJ solar cells, avoiding the use of In, which is a scarce metal with high cost. As for the solar cell

performance, we obtain higher  $J_{\text{SC}}$  (37.8  $\text{mA}/\text{cm}^2$  vs 37.3  $\text{mA}/\text{cm}^2$ ), comparable  $V_{\text{OC}}$  (0.737 V vs 0.734 V), and higher  $\text{FF}$  (79.1% vs 74.0%). The  $J_{\text{SC}}$  is higher because there is no reflection and absorption loss due to the encapsulation material. Comparable  $V_{\text{OC}}$  means equivalent passivation quality for these solar cells, while higher  $\text{FF}$  reveals lower  $R_s$ , which may be due to the better electric contact at the C/Cu-TCO interface compared with that at the InSn/Cu-TCO interface and/or the advantage of rear emitter cell structure.

In Figure 10F, we calculate the power loss ( $P_{\text{loss}}$ ) of the direct copper metallized cell depending on the C/Cu wire diameter and  $R_{\text{sheet,TCO}}$  at the front side of the cell. Here, the minimum  $P_{\text{loss}}$  is obtained by varying the number of C/Cu wire for the given C/Cu wire diameter and  $R_{\text{sheet,TCO}}$  at the front side of the cell, where  $P_{\text{loss}}$  is the sum of resistive loss ( $P_{\text{resistance}}$ ) and optical loss ( $P_{\text{shading}}$ ) of the simulated cell which can be calculated according to

$$P_{\text{resistance}} = R_s (J_{\text{mpp}})^2 \quad (6)$$

$$P_{\text{shading}} = A_{\text{shading}} J_{\text{mpp, no shading}} V_{\text{mpp}} \quad (7)$$

$R_s$ ,  $A_{\text{shading}}$ ,  $J_{\text{mpp}}$ , and  $V_{\text{mpp}}$  are the series resistance, C/Cu wire shading fraction, maximum power point current density, and voltage of the simulated cell, respectively.  $J_{\text{mpp, no shading}}$  is the maximum power point current density of the simulated cell without C/Cu wire shading.  $R_s$  is calculated as described earlier and is found rather small ( $<1$   $\Omega\text{-cm}^2$ ), which hardly impacts the maximum power point current

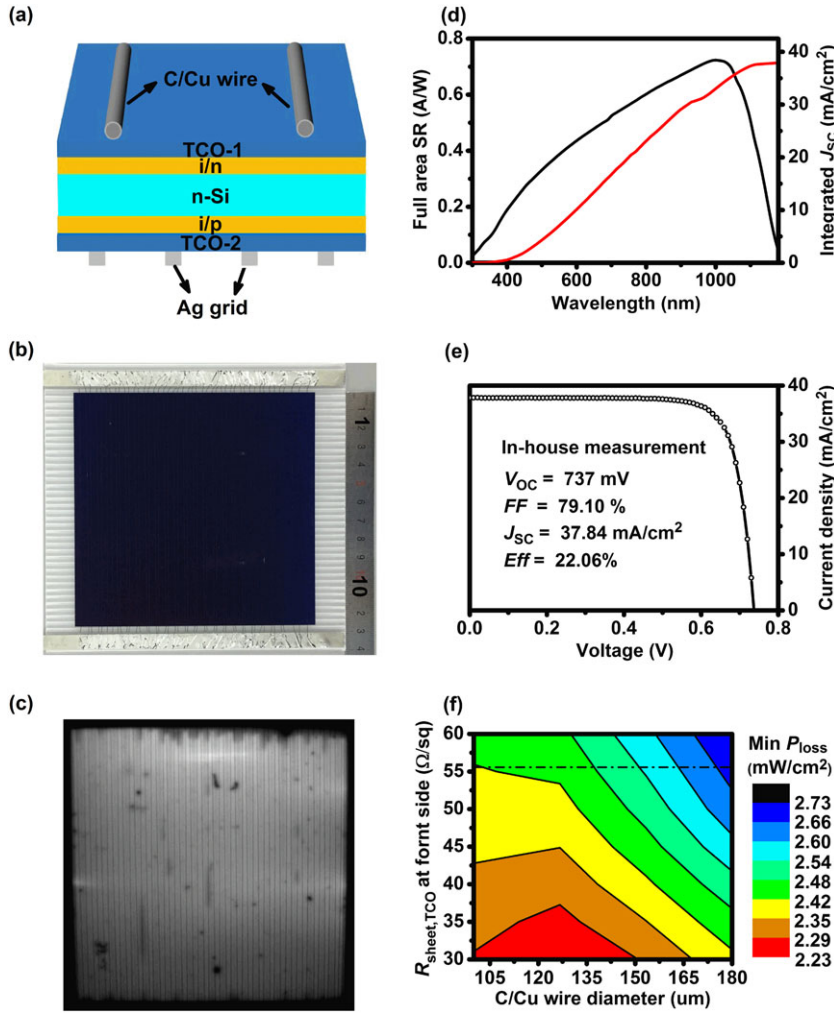


**FIGURE 10** Schematic cross section (A), photo (B), and EL image (C) of the proof of concept direct copper metallized rear emitter cell. (D) Full area SR from 300 to 1180 nm of the cell together with the integrated  $J_{sc}$  calculated by integrating the SR with AM 1.5G spectrum. (E) Light J-V curve of the cell. (F) Calculated minimum  $P_{loss}$  of the cell depending on C/Cu wire diameter and  $R_{sheet,TCO}$  at the front side of the cell. The dash line indicates  $R_{sheet,TCO}$  for our state-of-the-art process [Colour figure can be viewed at [wileyonlinelibrary.com](http://wileyonlinelibrary.com)]

density of the simulated cell. Hence,  $J_{mpp, no shading}$  and  $J_{mpp}$  can be calculated by

$$J_{mpp, no shading} = J_{mpp}^0 / (1 - A_{shading}^0) \quad (8)$$

$$J_{mpp} = J_{mpp, no shading} (1 - A_{shading}) \quad (9)$$

Herein,  $J_{mpp}^0$  is the measured maximum power point current density of the 22.06% cell, and  $A_{shading}^0$  is the C/Cu wire shading fraction of this cell. While  $V_{mpp}$  is calculated according to

$$V_{mpp} = V_{mpp}^0 - \Delta R_s J_{mpp} \quad (10)$$

$$\Delta R_s = R_s - R_s^0 \quad (11)$$

$V_{mpp}^0$  is the measured maximum power point current density of the 22.06% cell.  $\Delta R_s$  is the difference of calculated series resistance between the simulated cell and that of the 22.06% cell ( $R_s^0$ ). It can be found, for our state-of-the-art process, that the minimum  $P_{loss}$  of the direct copper metallized rear emitter cell can be reduced from  $\sim 2.5$  to  $\sim 2.4$  mW/cm<sup>2</sup> by decreasing the diameter of the C/Cu wire from 150 to  $\sim 105$   $\mu m$ , corresponding an  $Eff$  increase of  $\sim 0.1\%_{abs}$ , which will lead the  $Eff$  of the direct copper metallized cell close to its

screen-printed counterpart. Furthermore, another  $Eff$  gain of  $\sim 0.1\%_{abs}$  ( $P_{loss}$  reduce to  $\sim 2.3$  mW/cm<sup>2</sup>) is expected if the  $R_{sheet, TCO}$  at the front side of the cell can be reduced from 56 to  $\sim 30$   $\Omega/sq$  through improving the TCO mobility from 55 to 90 cm<sup>2</sup>/Vs as reported by Kobayashi et al.<sup>30</sup> and Meng et al.<sup>31</sup> It is worth noting that further work, like the thermal-cycling test, is still needed to evaluate the reliability of this metallization approach. Overall, the above results successfully demonstrate that high efficiency can also be realized in direct copper metallized rear emitter SHJ cells, which have potential to eliminate the use of silver paste completely and thus reduces the cost of SHJ solar cells dramatically.

## 4 | CONCLUSIONS

In summary, the development and optimization of the rear emitter SHJ solar cells have been investigated. The doping and thickness of the a-Si:H(p) layer are adjusted by varying B<sub>2</sub>H<sub>6</sub> flow and deposition time to enhance the emitter passivation without the restriction of parasitic absorption issue. The thickness of the a-Si:H(n) layer is tuned by adjusting the deposition time to suppress the absorption loss at the front side of the cell. The front and rear TCO layers are optimized separately by varying the oxygen partial pressure. The front TCO layer is

deposited at relatively high oxygen partial pressure to improve its optical performance while its requirement on conductivity is lowered because the lateral transport of the majority carriers at the front side of the cell can be shifted from TCO layer into the n-type Si substrate. The rear TCO layer is deposited at high oxygen partial pressure to suppress the TCO/a-Si:H(p) contact resistance. With all of these optimization, a 22.17% efficient rear emitter SHJ solar cell ( $225.47\text{cm}^2$ ,  $V_{OC} = 734\text{ mV}$ ,  $J_{SC} = 37.83\text{ mA/cm}^2$ ,  $FF = 79.84\%$ ) has been achieved with industry compatible process. Furthermore, we have investigated the possibility to metallize the rear emitter SHJ solar cell by soldering the C/Cu wires directly on front TCO layer and found that its series resistance can be well controlled. As a proof of concept, we have achieved a 22.06% efficient ( $156.25\text{ cm}^2$ ,  $V_{OC} = 737\text{ mV}$ ,  $J_{SC} = 37.84\text{ mA/cm}^2$ ,  $FF = 79.10\%$ ) rear emitter SHJ solar cell whose front side is directly copper metallized. It is further predicted that the direct copper metallized cell could yield equivalent efficiency as its screen-printed counterpart with achievable optimization. Overall, the direct copper metallized rear emitter SHJ solar cells open a promising approach for achieving high efficiency in low cost and thus can be a candidate for the mass production of SHJ solar cells.

## ACKNOWLEDGEMENTS

This work was supported by the National 863 Program 2011AA050502, the National Natural Science Foundation of China (grant nos. 61234005, 11474201, and 11674225), the Postdoctoral Science Foundation of Jiangsu Province, and the Program for Innovation and Entrepreneurship of Jiangsu Province.

## ORCID

Lifei Yang  <http://orcid.org/0000-0001-6417-194X>

## REFERENCES

- Taguchi M, Yano A, Tohoda S, et al. 24.7% record efficiency HIT solar cell on thin silicon wafer. *IEEE J Photovoltaics*. 2013;4:96-99.
- Mishima T, Taguchi M, Sakata H, Maruyama E. Development status of high-efficiency HIT solar cells. *Sol Energy Mater Sol Cells*. 2011;95:18-21.
- Battaglia C, Cuevas A, Wolf SD. High-efficiency crystalline silicon solar cells: status and perspectives. *Energ Environ Sci*. 2016;9:1552-1576.
- Adachi D, Hernández JL, Yamamoto K. Impact of carrier recombination on fill factor for large area heterojunction crystalline silicon solar cell with 25.1% efficiency. *Appl Phys Lett*. 2015;107: 233506-1-233506-3.
- Yoshikawa K, Kawasaki H, Yoshida W, et al. Silicon heterojunction solar cell with interdigitated back contacts for a photoconversion efficiency over 26%. *Nat Energy*. 2017;2: 17032-1-17032-8.
- Chavali RV, Johlin EC, Gray JL, Buonassisi T, Alam MA. A framework for process-to-module modeling of a-Si/c-Si (HIT) heterojunction solar cells to investigate the cell-to-module efficiency gap. *IEEE J Photovoltaics*. 2016;6:875-887.
- Bivour M, Schröer S, Hermle M, Glunz SW. Silicon heterojunction rear emitter solar cells: less restrictions on the optoelectrical properties of front side TCOs. *Sol Energy Mater Sol Cells*. 2014;122:120-129.
- Bivour M, Steinkemper H, Jeurink J, Schröer S, Hermle M. Rear emitter silicon heterojunction solar cells: fewer restrictions on the optoelectrical properties of front side TCOs. *Energy Procedia*. 2014;55:229-234.
- Watahiki T, Furuhashi T, Matsuura T, et al. Rear-emitter Si heterojunction solar cells with over 23% efficiency. *Appl Phys Express*. 2015;8: 021402-1-021402-3.
- Kobayashi E, Watabe Y, Hao R, Ravi TS. Heterojunction solar cells with 23% efficiency on n-type epitaxial kerfless silicon wafers. *Prog Photovoltaics Res Appl*. 2016;24:1295-1303.
- Louwen A, Van Sark W, Schropp R, Faaij AA. Cost roadmap for silicon heterojunction solar cells. *Sol Energy Mater Sol Cells*. 2016;147:295-314.
- Levrat J, Thomas K, Faes A, Champlaud J, Allebé C, Badel N, Barraud L, Debrot F, Descoedres A, Lachowicz A, Kiaee M, Despeisse M, Ballif C. Metal-free crystalline silicon solar cells in module. *IEEE 42nd Photovoltaic Specialist Conference*, 2015.
- Rendler LC, Walter J, Kraft A, Ebert C, Wiese S, Eitner U. Ultra-soft wires for direct soldering on finger grids of solar cells. *Energy Procedia*. 2017;124:478-483.
- Despeisse M, Ballif C, Faes A, Lachowicz A. Metallization and interconnection for silicon heterojunction solar cells and modules. *Photovoltaics International*. 2016;30:1-5.
- Descoedres A, Allebé C, Badel N, et al. Silicon heterojunction solar cells: towards low-cost high-efficiency industrial devices and application to low-concentration PV. *Energy Procedia*. 2015;77:508-514.
- Jensen N, Rau U, Hausner RM, Uppal S, Oberbeck L, Bergmann RB. Recombination mechanisms in amorphous/crystalline silicon heterojunction solar cells. *J Appl Phys*. 2000;87:2639-2645.
- Powell MJ, Deane SC. Improved defect-pool model for charged defects in amorphous silicon. *Phys Rev B*. 1993;48:10815-10827.
- Wolf SD, Kondo M. Nature of doped a-Si:H/c-Si interface recombination. *J Appl Phys*. 2009;105: 103707-1-103707-6.
- Bivour M, Sebastian S, Martin H. Numerical analysis of electrical TCO/a-Si:H(p) contact properties for silicon heterojunction solar cells. *Energy Procedia*. 2013;38:658-669.
- Fujiwara H, Kondo M. Effects of a-Si:H layer thicknesses on the performance of a-Si:H/c-Si heterojunction solar cells. *J Appl Phys*. 2007;101: 054516-1-054516-9.
- Khanna A, Mueller T, Stangl RA, Bram H, Basu PK, Aberle AGA. Fill factor loss analysis method for silicon wafer solar cells. *IEEE J Photovoltaics*. 2013;3:1170-1177.
- Holman ZC, Descoedres A, Barraud L, et al. Current losses at the front of silicon heterojunction solar cells. *IEEE J Photovoltaics*. 2012;2:7-15.
- Ritzau KU, Behrendt T, Palaferri D, Martin B, Hermle M. Hydrogen doping of indium tin oxide due to thermal treatment of hetero-junction solar cells. *Thin Solid Films*. 2016;599:161-165.
- Gogolin R, Turcu M, Ferré R, et al. Analysis of series resistance losses in a-Si:H/c-Si heterojunction solar cells. *IEEE J Photovoltaics*. 2014;4:1169-1176.
- Eideloth S, Brendel R. Analytical theory for extracting specific contact resistances of thick samples from the transmission line method. *IEEE Electron Device Lett*. 2014;35:9-11.
- Mette A. *New Concepts for Front Side Metallization of Industrial Silicon Solar Cells*. Freiburg, Germany: Ph.D. thesis, Univ. Freiburg; 2007:16-17.
- Haug FJ, Biron R, Kratzer G, et al. Improvement of the open circuit voltage by modifying the transparent indium-tin oxide front electrode in amorphous n-i-p solar cells. *Prog Photovoltaics Res Appl*. 2012;20:727-734.
- Lee SY, Choi H, Li HM, et al. Analysis of a-Si:H/TCO contact resistance for the Si heterojunction back-contact solar cell. *Sol Energy Mater Sol Cells*. 2014;120:412-416.
- Lachenal D, Baetzner D, Frammelsberger W, et al. Heterojunction and passivated contacts: a simple method to extract both n/tco and p/tco contacts resistivity. *Energy Procedia*. 2016;92:932-938.

30. Kobayashi E, Watabe Y, Yamamoto T, Yamada Y. Cerium oxide and hydrogen co-doped indium oxide films for high-efficiency silicon heterojunction solar cells. *Sol Energy Mater Sol Cells*. 2016;149:75-80.
31. Meng FY, Shi JH, Liu ZX, Cui YF, Lu ZD, Feng ZQ. High mobility transparent conductive W-doped  $\text{In}_2\text{O}_3$  thin films prepared at low substrate temperature and its application to solar cells. *Sol Energy Mater Sol Cells*. 2014;122:70-74.

**How to cite this article:** Yang L, Zhong S, Zhang W, et al. Study and development of rear-emitter Si heterojunction solar cells and application of direct copper metallization. *Prog Photovolt Res Appl*. 2018;26:385-396. <https://doi.org/10.1002/pip.3000>